RSC Advances

PAPER

View Article Online
View Journal | View Issue

Cite this: *RSC Adv.*, 2024, **14**, 7124

Ball milling synthesis of Fe_3O_4 nanoparticles-functionalized porous boron nitride with enhanced cationic dye removal performance†

Jie Li,[ab] Chuanhui Wang,[ab] Xinqi Chen,[ab] Yunxiu Ma,[ab] Chu Dai,[ab] Hui Yang,[ab] Qian Li,[b] Junhui Tao*[ab] and Tian Wu[ab]

Enhancement of the adsorption performance and recyclability of adsorbents is a crucial aspect of water treatment. Herein, we used one-dimensional porous boron nitride (PBN) as a carrier to load Fe_3O_4 nanoparticles for the preparation of Fe_3O_4 nanoparticles-functionalized porous boron nitride (Fe_3O_4/PBN) *via* a ball milling method. The high-energy ball milling promoted the creation of a negatively charged PBN surface and facilitated the uniform distribution of Fe_3O_4 nanoparticles on the surface of PBN. The adsorption performance of Fe_3O_4/PBN toward cationic dyes could be significantly improved while no enhancement was observed for anionic dyes. The great adsorption performance of Fe_3O_4/PBN is due to its surface functional groups and surface defects formed in the ball milling process. Moreover, the strong interaction force between Fe_3O_4/PBN and cationic dyes promotes rapid initial adsorption due to their negatively charged surface. Magnetic measurements demonstrated that Fe_3O_4/PBN is superparamagnetic. The composites with low loadings of Fe_3O_4 nanoparticles could be quickly separated from the aqueous solution under a low applied magnetic field, improving their recyclability. This work highlights the role of ball milling in improving the adsorption performance of Fe_3O_4/PBN and greatly promotes the practical application of Fe_3O_4/PBN in the field of environmental purification.

Received 6th November 2023
Accepted 23rd January 2024

DOI: 10.1039/d3ra07557e

rsc.li/rsc-advances

1. Introduction

Developing novel materials and advanced technologies to effectively eliminate pollutants from water has great scientific significance and great value in practical applications for solving global environmental issues.[1,2] Adsorption has been considered to be one of the most efficient methods for water treatment due to its simple operation, low cost and it being an environmentally friendly method.[3–5] In particular, adsorption has obvious advantages for cleaning wastewater with low concentrations of pollutants as compared to chemical settlement, biodegradation, and membrane filtration.[6] Effective adsorption has been demonstrated using activated carbon, magnetic biosorbents, natural coagulants, and other nano-composites.[7–9] Activated carbon has been widely used in the field of environmental purification.[10,11] However, these materials cannot fully clean wastewater with increasingly complex components due to their disadvantages, such as low adsorption capacity, poor chemical stability, and low regeneration efficiency.[12,13] Thus, there is an urgent need to develop efficient, stable and safe adsorption materials to solve the problem of water pollution.

Porous boron nitride (PBN) has been considered as an ideal adsorption and support material because of its large specific surface area, high thermal stability, and good chemical inertia.[14–18] Various synthetic efforts have already been undertaken for the creation of PBN. Even so, PBN has mostly existed in a powder state, thus making it difficult to separate from wastewater after adsorption.[19–22] Poor recyclability has limited its practical application in the field of water treatment. The combination of PBN with magnetic nanomaterials to prepare composite adsorbents is an effective strategy to solve this problem. Significantly, Fe_3O_4 nanoparticles with excellent magnetic properties and low biological toxicity have aroused widespread interest for use in water treatment.[23,24]

Herein, we report ball-milled Fe_3O_4/PBN for enhancing wastewater purification, where one-dimensional PBN with large specific surface area and high stability acts as a support to load Fe_3O_4 nanoparticles with average diameters of ~25 nm. The negatively charged PBN, effectively created by high-energy ball milling, was not only conducive for enhancing the adsorption of a cationic dye but also helped to uniformly anchor Fe_3O_4 nanoparticles on the surface of PBN. The excellent synergistic adsorption of the cationic dye on Fe_3O_4/PBN was closely related

[a]*School of Physics and Mechanical & Electronical Engineering, Institute for Functional Materials, Hubei University of Education, Wuhan 430205, P.R. China. E-mail: junhuitao@hue.edu.cn; Fax: +86-27-52363361; Tel: +86-27-52363361*

[b]*Institute of Materials Research and Engineering, Hubei Expert Workstation for Terahertz Technology and Advanced Energy Materials and Devices, Hubei University of Education, Wuhan 430205, P.R. China*

† Electronic supplementary information (ESI) available: Effect of temperature on the adsorption performance of Fe_3O_4/PBN1 for MB. See DOI: https://doi.org/10.1039/d3ra07557e

to Fe_3O_4 nanoparticle loading content and the use of a high-energy ball milling method. Compared to pure PBN, the negatively charged ball-milled PBN exhibited stronger electrostatic forces with cationic dye, leading to the preferential adsorption of the cationic dye. Moreover, Fe_3O_4/PBN could be easily manipulated, even at a low magnetic field, due to their superparamagnetism. This feature effectively overcame the disadvantage of powdered PBN, which is not easily separated from water after adsorption, increasing the recyclability of Fe_3O_4/PBN. The role of ball milling and the mechanism by which the cationic dye is adsorbed over Fe_3O_4/PBN were discussed.

2. Experimental

2.1 Synthesis

All chemicals were of analytical grade and were directly used without further purification. In a typical synthesis process, 7.42 g of H_3BO_3 and 7.56 g of $C_3N_6H_6$ were added in 200 mL of deionized water and heated at 85 °C for 2 h followed by natural cooling to room temperature to obtain a white precursor ($C_3N_6H_6 \cdot 2H_3BO_3$). Subsequently, the as-prepared precursor was heated to 1000 °C at a rate of 10 °C min^{-1} and kept there for 3 h in a flow of N_2 to obtain the white PBN product.

Fe_3O_4/PBN was synthesized from as-prepared PBN and Fe_3O_4 nanoparticles with average diameters of ~25 nm through a high-energy ball milling method. First, 5.0 g of PBN were placed into a ball mill tank containing zirconia balls with three different sizes at room temperature; second, a certain mass ratio of Fe_3O_4 nanoparticles to PBN (1 wt%, 5 wt%, 10 wt%) was added into the ball mill tank (QM-1F, China) and mixed with 20 mL of ethanol, following high-energy ball milling at 550 rpm for 6 h; finally, wet powders were heat-treated at 80 °C for 2 h to obtain Fe_3O_4/PBN. According to the different mass ratios of Fe_3O_4 nanoparticles to PBN, samples were marked as: Fe_3O_4/PBN1, Fe_3O_4/PBN2, and Fe_3O_4/PBN3.

2.2 Characterization

The crystal structures of PBN and Fe_3O_4/PBN were detected using powder X-ray diffraction (XRD, Shimadzu XRD-6100). Scanning electron microscopy (SEM, Hitachi S-4800) and transmission electron microscopy (TEM, Philips TECNAI-20) were applied to observe and analyze the micro-morphology and surface structure of samples. The elemental maps for C, B, N, O, and Fe were obtained using energy dispersive spectroscopy (EDS). The chemical bonds of composites were analyzed to understand the chemical composition and functional groups present using Fourier-transform infrared spectroscopy (FTIR, Bruker Tensor 27). To study the specific surface area and porous characteristics of samples, low temperature (77 K) nitrogen adsorption/desorption isotherms were obtained using an autoSorb Quantachrome instrument (Quantachrome Ins, Autosorb-iQ-1900). Magnetization curves of samples at room temperature were measured using a vibrating sample magnetometer (VSM, LakeShore VSM-7404). The pH values of aqueous solutions were detected on a pH meter (PHS-25, Hangzhou). The concentrations of dyes in aqueous solutions were determined using a UV-visible spectrophotometer (UV/vis, Shimadzu UV-2600).

2.3 Batch adsorption experiments

Organic dyes, such as methylene blue (MB, cationic dye) and methyl orange (MO, anionic dye), were selected as model pollutants. An appropriate amount of organic dye was dissolved in deionized water and diluted to the required concentration for adsorption experiments. To assess the adsorption rate of organic dyes on Fe_3O_4/PBN, samples (50 mg) were added to 200 mL of a MB water solution with a concentration of 50 mg L^{-1} at a pH value of 8 at 20 °C. To study the effect of temperature on the adsorption performance, the water temperature was varied from 10 to 50 °C. To evaluate the effect of pH on the adsorption performance, the pH values of the aqueous solution were adjusted from 2.0 to 12.0 by adding an appropriate amount (0.1 mol L^{-1}) of HNO_3 and NaOH solutions. For comparison, the adsorption properties of MO on Fe_3O_4/PBN were tested under same experimental conditions.

The contaminant removal efficiency is calculated from the following formula:

$$\eta(\%) = (C_0 - C_e)100/C_0, \quad (2.1)$$

where, C_0 and C_e (mg L^{-1}) represent the equilibrium concentrations of the contaminant in the wastewater before and after adsorption experiments. η is the percentage of organic dye removed from the wastewater.

The Langmuir model can be expressed as a formula:

$$Q_e = Q_m K C_e/(1 + KC_e), \quad (2.2)$$

where Q_e (mg g^{-1}) represents the adsorption amount per unit adsorbent for wastewater at adsorption equilibrium; Q_m (mg g^{-1}) represents the adsorption capacity of the adsorbent; C_e (mg L^{-1}) is the concentration of the contaminant in wastewater at adsorption equilibrium; and K (L mg^{-1}) is the equilibrium constant of the Langmuir adsorption.

Fe_3O_4/PBN with adsorbed MB was efficiently separated from aqueous solutions within 3 min under a low external magnetic field. The regeneration of used samples was carried out using a catalytic degradation method with the assistance of H_2O_2.

3. Results and discussion

3.1 Characterization

A representative SEM image of pure PBN prepared at 1000 °C under N_2 flow is shown in Fig. 1a. The pure PBN exhibits a regular ribbon-like morphology with the main length falling in the range of 3 to 20 μm, the width between 0.3–3 μm and the thickness between 200–600 nm. The surface of ribbon-like PBN is smooth. Occasionally, some fragmentation of PBN is also observed. The morphology of ball-milled PBN shows no obvious change in general, as displayed in Fig. 1b. However, the surface of ball-milled PBN becomes rough, and the amount of PBN grains increase due to the milling cutting force. Significantly, Fe_3O_4 nanoparticles were uniformly anchored on the surface of

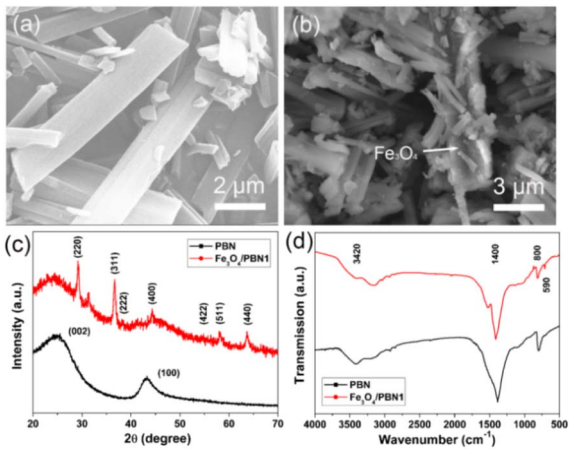

Fig. 1 (a) SEM image of PBN. (b) SEM image of Fe_3O_4/PBN1 indicating the uniform dispersion of Fe_3O_4 nanoparticles on the surface of PBN. (c) XRD patterns and (d) FTIR spectra of pure PBN and Fe_3O_4/PBN1.

PBN (marked by arrows), which was mainly caused by surface defects and hydroxyl groups formed in the ball milling process. The crystalline structures of pure PBN and Fe_3O_4/PBN1 were characterized using XRD, as depicted in Fig. 1c. The two major diffraction peaks of pure PBN at ~26° and 42.5° can be attributed to the (002) and (100) crystal planes of hexagonal BN (JCPDS no. 45-0896), respectively.[25,26] Besides the major diffraction peaks of Fe_3O_4/PBN1, diffraction peaks at about 30.1°, 35.4°, 37.2°, 43.1°, 53.3°, 56.9° and 62.5° can be indexed to the (220), (311), (222), (400), (422), (511), (440) crystal planes of cubic Fe_3O_4 (JCPDS no. 11-0614).[27] These findings indicate that the crystalline structure of PBN was not obviously destroyed during the ball milling process. In addition, Fig. S1a† illustrates that the relative intensities of XRD peaks belonging to Fe_3O_4 were enhanced with increased loading of Fe_3O_4 nanoparticles. The FTIR spectra in Fig. 1d show the main peaks of the two samples at about 1400 and 800 cm^{-1} and are indexed to B–N stretching vibrations and B–N–B bending vibrations.[28,29] The intensity of vibration bands of ball-milled PBN at ~3420 and ~1630 cm^{-1} corresponding to stretching and bending vibrations of hydroxyl groups became stronger than those in pure PBN, revealing that the number of hydroxyl groups increased. The negatively charged PBN surface helps to enhance the adsorption of cationic dyes and interaction force between Fe_3O_4 nanoparticles and ball-milling PBN.[30] The new peak in the Fe_3O_4/PBN1 spectrum located at ~590 cm^{-1} is attributed to the Fe–O stretching vibration of Fe_3O_4 nanoparticles,[23] indicating that Fe_3O_4 nanoparticles were anchored on the PBN surface. The intensities in the FTIR spectra in Fig. S1b† corresponding to the Fe–O bands of Fe_3O_4/PBN2 and Fe_3O_4/PBN3 were improved relative to Fe_3O_4/PBN1 due to the presence of more Fe_3O_4 nanoparticles in these samples. Based on the above experimental results, Fe_3O_4/PBN had been successfully prepared using the ball milling method. The strengthened adsorption activity may mainly be ascribed to the presence of ball-milled PBN.

SEM images of Fe_3O_4/PBN1, Fe_3O_4/PBN2 and Fe_3O_4/PBN3 are displayed in Fig. 2a–c, respectively. Evidently, Fe_3O_4/PBN1 (Fig. 2a) was sparsely loaded with Fe_3O_4 nanoparticles, while more Fe_3O_4 nanoparticles (Fig. 2c) were loaded on the surface of PBN in Fe_3O_4/PBN3. It is observed from Fig. 2a–c that Fe_3O_4 nanoparticles were uniformly and firmly anchored to the surface of PBN without obvious self-agglomeration due to hydroxyl groups and surface defects resulting from the high-energy ball milling process.[31,32] In addition, micro-morphologies and micro-structure of Fe_3O_4 nanoparticles and PBN show no obvious change before and after ball milling. The TEM image of Fe_3O_4/PBN1further confirms that Fe_3O_4 nanoparticles were directly anchored to the surface of ribbon-like PBN (marked by arrows), as shown in Fig. 2d. Moreover, the elemental distributions on the Fe_3O_4/PBN micro-ribbon were analyzed using energy dispersive spectroscopy (EDS). The corresponding C, B and N elemental maps (Fig. 2e–g) clearly indicate that the distributions of C, B and N elements are uniform. The oxygen and iron elements (Fig. 2h and j) are indeed present and also uniformly distributed over the Fe_3O_4/PBN micro-ribbon. These results reveal that Fe_3O_4 nanoparticles were uniformly loaded on ball-milled PBN. The numerous surface defects of ball-milled PBN were produced by the milling cutting force since PBN layers are bound by van der Waals type forces.[31] Significantly, the surface defects of ball-milled PBN could serve as activated sites for the adsorption of pollutants and good distribution of Fe_3O_4 nanoparticles.

Fig. 3a shows nitrogen adsorption/desorption isotherms for Fe_3O_4/PBN1 and pure PBN at 77 K. According to the International Union of Pure and Applied Chemistry nomenclature, the low temperature nitrogen adsorption/desorption isotherms of pure PBN and Fe_3O_4/PBN1 can be classified as a class type-I isotherm and an H4 type broad hysteresis loop, respectively.[33] This suggests that the porous structures of pure PBN and Fe_3O_4/

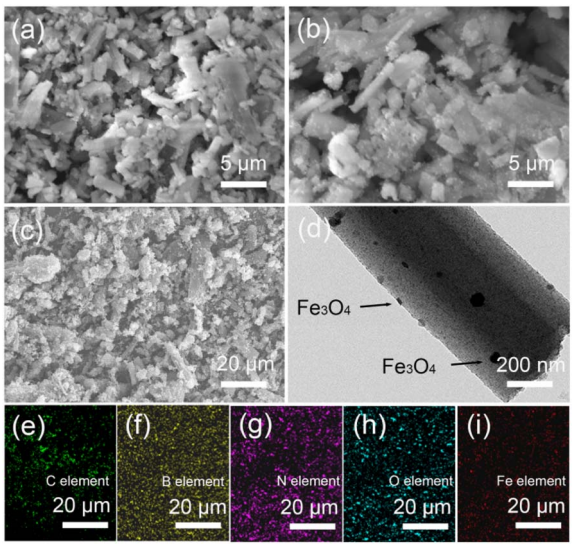

Fig. 2 (a) SEM image of Fe_3O_4/PBN1. (b) SEM image of Fe_3O_4/PBN2. (c) SEM image of Fe_3O_4/PBN3. (d) TEM image of Fe_3O_4/PBN1. (e–i) Elemental maps for C, B, N, O, and Fe.

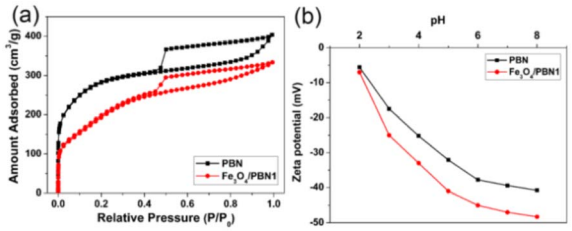

Fig. 3 (a) Low temperature nitrogen adsorption/desorption isotherms for pure PBN and Fe_3O_4/PBN1. (b) Zeta-potential *vs.* pH for pure PBN and Fe_3O_4/PBN1.

PBN1 are mainly composed of slit-shaped mesopores and micropores. The porous structure of as-prepared ball-milled PBN was not obviously destroyed, which was consistent with SEM and TEM observations. The amount of N_2 adsorbed on Fe_3O_4/PBN1 in the low pressure range was lower than that of PBN, indicating that some micro-/mesopores were blocked or disappeared during the ball milling process. The specific surface areas of pure PBN and Fe_3O_4/PBN1 were 952 and 861 m^2 g^{-1}, respectively, as calculated using the Brunauer–Emmett–Teller (BET) formula.[34] Their pole volumes were 0.52 and 0.46 cm^3 g^{-1} based on the Langmuir model, respectively.[35]

The surfaces of pure PBN and Fe_3O_4/PBN1 exhibit negative charges at pH values ranging from 2 to 8, due to the presence of hydroxyl groups and surface defects, as shown in Fig. 3b. The zeta-potential values of the two samples increase as pH values increase. It is noticeable that the zeta-potential values of Fe_3O_4/PBN1 were higher than those of pure PBN at same pH values because more hydroxyl groups and surface defects were introduced on Fe_3O_4/PBN1 during the ball milling process. As a result, the zeta-potential value of Fe_3O_4/PBN1 reached −47.1 eV at pH 7. The high zeta-potential value is conducive to promoting the adsorption of MB because of improved electrostatic attraction between Fe_3O_4/PBN1 and the cationic dye.[36]

Fig. 4 shows the magnetic properties of Fe_3O_4/PBN1 at room temperature. Their saturated magnetization was 2.9 emu g^{-1}. The curve is almost without hysteresis and reveals that Fe_3O_4/PBN1 has superparamagnetic properties due to small-sized Fe_3O_4 nanoparticles being uniformly anchored to ball-milled PBN with no obvious self-agglomeration.[37] The initial solution containing Fe_3O_4/PBN1 was placed in an external magnetic field, which became quickly clear within 3 min, as shown in the inset. Apparently, Fe_3O_4/PBN1 in the aqueous solution was quickly attracted on the side wall of the bottle, thus showing that the recycling efficiency of PBN was improved.

3.2 Adsorption studies

Because of its high specific surface area, large pore volume, good chemical stability and numerous surface negative charges, Fe_3O_4/PBN was the ideal adsorption and support material for wastewater treatment. MB and MO contain aromatic rings and were used as organic contaminants to assess the performance of Fe_3O_4/PBN for water treatment. In addition, the effects of experimental parameters on the adsorption of organic dyes were investigated in detail.

To elucidate the effect of the ball milling and loading of Fe_3O_4 nanoparticles have on the adsorption ability of Fe_3O_4/PBN, a series of comparative experiments on water purification were performed. The MB removal percentages of different adsorbents in an aqueous solution are shown in Fig. 5. The cationic dye removal rate for pure PBN was rapid and reached saturation adsorption within only 50 min, 88.9 wt% of MB was removed from the aqueous solution. For Fe_3O_4/PBN1 with a sparse loading of Fe_3O_4 nanoparticles, 92.3 wt% of MB was effectively removed from the aqueous solution within the initial 5 min. The MB adsorption equilibrium of Fe_3O_4/PBN1 was approached within 50 min with a removal percentage of up to 99.7 wt%. The excellent adsorption performance was mainly due to numerous functional groups and surface defects formed during the ball milling process. Interestingly, the MB removal percentage of Fe_3O_4/PBN2 rapidly increased in the first 10 min, then the adsorption rate of MB gradually slowed down. However, adsorption equilibrium was not reached even within 360 min. The MB adsorption rate of Fe_3O_4/PBN3 with a dense loading of Fe_3O_4 nanoparticles was slow throughout the

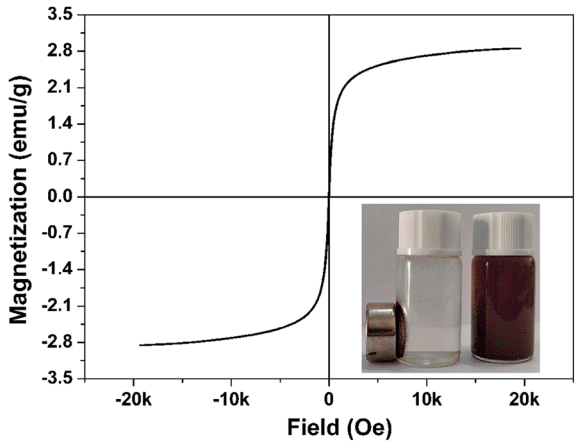

Fig. 4 Magnetization curve of Fe_3O_4/PBN1 at room temperature. Inset shows a photograph of the aqueous solution of Fe_3O_4/PBN1 before and after the application of an external magnetic field.

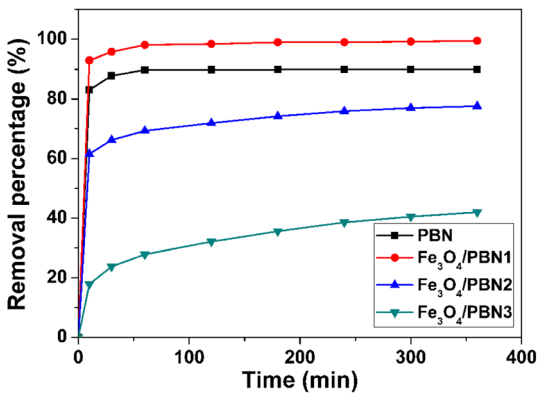

Fig. 5 MB removal percentages on different adsorbents (pH value: 7, adsorbent dosage: 50 mg, dye concentration: 50 mg L^{-1}, and adsorption temperature: 20 °C).

adsorption process. This was mainly due to the following two reasons: first, adsorption active sites in Fe_3O_4/PBN3 decreased due to Fe_3O_4 nanoparticles being loaded on the surface of PBN; second, the electrostatic attraction between Fe_3O_4 nanoparticles and the cationic dye was weak. The adsorption capacities of the four adsorbents followed the order, Fe_3O_4/PBN1 > PBN > Fe_3O_4/PBN2 > Fe_3O_4/PBN3. Experimental results revealed that the adsorption behavior was strongly correlated with the ball milling process and the mass ratio of Fe_3O_4 NPs to BNNSs in composites.

The adsorption rate of Fe_3O_4/PBN2 was very fast during the initial phase due to the preferential adsorption of MB onto ball-milled PBN. However, the next slow adsorption phase revealed that the adsorption of MB on Fe_3O_4 nanoparticles played a main role. The synergistic adsorption of MB on Fe_3O_4/PBN arose from two aspects: the strong electrostatic interaction between ball-milled PBN and MB caused the initial rapid adsorption by Fe_3O_4/PBN2, while the weak electrostatic force between Fe_3O_4 nanoparticles and MB resulted in long interaction times. The low interaction between cationic dyes and Fe_3O_4 nanoparticles is a major rate-limiting factor throughout the synergistic adsorption process. In addition, the magnetic properties of Fe_3O_4/PBN mean that it is easy to separate from an aqueous solution under an external magnetic field, thus improving the recycling efficiency.

Fig. 6a displays the MB and MO removal percentages of Fe_3O_4/PBN1. MB was quickly removed from the aqueous solution within the initial 5 min and obtained adsorption equilibrium within 50 min. The MB removal percentage was up to 99.7 wt%. However, MO adsorption equilibrium over Fe_3O_4/PBN1 was not reached, even within 180 min under same experimental conditions. Only 67 wt% of MO was removed, and the adsorption rate was decreased as time went on. This high adsorption of MB reveals that the adsorption active sites of Fe_3O_4/PBN possess good mutual adhesion ability with MB molecules due to the negatively charged PBN surface.[38]

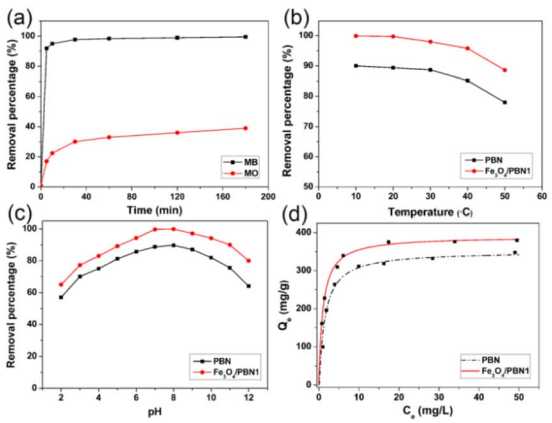

Fig. 6 (a) Effect of the charge of the organic dye on the adsorption performance of Fe_3O_4/PBN1. (b) Effect of temperature on the MB adsorption performance of two adsorbents. (c) Effect of pH on the MB adsorption performance of two adsorbents. (d) MB adsorption isotherms on pure PBN and Fe_3O_4/PBN1.

Fig. 6b shows the effect of changing solution temperatures from 10 to 50 °C has on the adsorption capacities of pure PBN and Fe_3O_4/PBN1. When the solution temperature was 10 °C, 99.9 wt% of MB in the aqueous solution was effectively removed by Fe_3O_4/PBN1. As the temperature of the solution increased, the removal ability of composites was gradually weakened, and the removal percentage was only 88.6 wt% at 50 °C. These results indicate that the adsorption process was an exothermic process.

However, the time to reach adsorption equilibrium was significantly shortened when the solution temperature was increased, revealing that increasing the adsorption temperature helps to improve the adsorption rate, as shown in Fig. S2.† This can be understood by considering the following points: increasing temperature can improve the diffusion rate of organic dye molecules on the surface and in the pores of Fe_3O_4/PBN1; increasing temperature can enhance the equilibrium adsorption capacity of the adsorbent for organic dye molecules in an aqueous solution. The pure PBN also showed similar MB adsorption performance.

Testing the effect of the solution pH on the adsorption performance of Fe_3O_4/PBN1 is important to fully assess the value of composites in the field of water treatment. As shown in Fig. 6c, when the solution was at pH 2, the MB removal percentage of Fe_3O_4/PBN1 was as much as 65 wt%; the removal performance was enhanced with an increase in pH values. As a result, the adsorption capacity of composites reached a maximum value of up to 99.9 wt% at pH of 7, and MB in the aqueous solution was almost completely removed. When the pH of the solution was more than 8, the removal ability of composites gradually decreased. However, 80 wt% of the removal capacity remained, even at pH 12.

At the same time, we also studied the MB adsorption performance of Fe_3O_4/PBN1 in different water sources, including distilled water, tap water, Yangtze River water and local pond water. As shown in Fig. S3,† the MB removal efficiencies of Fe_3O_4/PBN1 decreased to about 91.2%, 80.6%, and 65.7% in comparison with the control experiment (distilled water). This is because of the competition with the total dissolved organic material and coexisting cations for adsorption sites.

The difference in the surface charge between adsorbents and pollutants contributes to the enhancement of the MB adsorption performance of Fe_3O_4/PBN1. The adsorption capacity of Fe_3O_4/PBN1 gradually improved with increasing pH when the pH < 7. There were more negatively charged OH^- groups and nitrogen-defect sites on the surface of Fe_3O_4/PBN1 when the solution pH increased which was conducive to the adsorption of the cationic dye. However, excessive negative charge in the aqueous solution hindered the ability of cationic dye molecules to diffuse to the surface or the pores of Fe_3O_4/PBN1 when the pH > 7, resulting in a decreased adsorption capacity.[35] Overall, Fe_3O_4/PBN1 can be widely used in the field of water purification under hazardous environments. A reasonable explanation for this is that large number of hydroxyl groups and boron atom vacancies on its surface provide abundant negative charges. Electrostatic attraction between MB (cationic dye) and

negatively charged nitrogen atoms at the edges of ball-milled PBN plays an important role in the adsorption. The boron atom vacancies may be highly absorbent due to three unsaturated nitrogen atoms at these sites, which constitute a negatively charged N hole to trap MB cationic dye through electrostatic interactions, as shown in Fig. S4.† In addition, the hydroxyl groups on the Fe_3O_4/PBN surface revealed in the FTIR spectra may contribute to MB adsorption through an ion exchange reaction.[39]

Adsorption isotherms are widely used to analyze the adsorption characteristics of solid adsorbents for the removal of contaminants in an aqueous solution. Fig. 6d shows the MB adsorption isotherms of Fe_3O_4/PBN1 and pure PBN in an aqueous solution at pH 7 and at 20 °C. The concentration ranged from 0.3 to 50 mg L^{-1} during the adsorption process. The MB adsorption curves of Fe_3O_4/PBN1 and pure PBN were fitted using the Langmuir formula. It can be observed that the adsorption data were fitted by the Langmuir model (correlation coefficients, $R^2 > 0.99$). Based on the Langmuir model, the maximum MB adsorption capacities of Fe_3O_4/PBN1 and pure PBN in the aqueous solution were 393.5 and 331.7 mg g^{-1}, respectively. The removal capacity of Fe_3O_4/PBN1 was higher than that of most BN materials previously reported.[4,21,30,40,41] This result reveals that ball milling can be an attractive strategy to enhance adsorption performance by taming the dispersion of Fe_3O_4 nanoparticles and negatively charged PBN. The curve indicates that Fe_3O_4/PBN1 is still able to remove MB at very low concentrations. In addition, a simple regeneration experiment (catalytic degradation method with the assistance of H_2O_2) was carried out for the regeneration of the used Fe_3O_4/PBN material.[30] Batches of regeneration experiments were carried out on Fe_3O_4/PBN1 samples to evaluate their cycling performance for MB removal. The removal efficiency of about 86.3% was still retained even after 10 adsorption–regeneration cycles, as presented in Fig. S5.† It should be noted that the removal efficiency of Fe_3O_4/PBN1 after the fifth cycle was not obviously changed with a further increase of cycles. In addition, the zeta-potential value of Fe_3O_4/PBN1 reached −42.4 mV at pH 7, even after 10 runs (Fig. S6†), indicating that numerous negative charges on the surface of Fe_3O_4/PBN remained.

4. Conclusions

In summary, Fe_3O_4/PBN was successfully synthesized *via* a ball milling method, where the ball-milled PBN was used as a carrier for loading Fe_3O_4 nanoparticles. The resulting magnetic Fe_3O_4/PBN1, with sparsely loaded Fe_3O_4 nanoparticles, not only exhibited excellent adsorption performance toward cationic dyes as high as 393.5 mg g^{-1} but also possessed high recycling efficiency and could be effectively separated from water within 3 min. The enhanced adsorption performance and recyclability could be attributed to the high dispersion of Fe_3O_4 nanoparticles and negative charges on the PBN surface created by the ball milling process. In addition, the synergistic adsorption properties of Fe_3O_4/PBN toward MB were studied. We believe that this study can provide new insight into the design and synthesis of adsorbents for water treatment.

Author contributions

J. Li and J. H. Tao conceived and designed the experiments. C. H. Wang, X. Q. Chen, Y. X. Ma, C. Dai, H. Yang, Q. Li and T. Wu performed the experiments and analyzed the data. J. Li and J. H. Tao wrote the manuscript. All authors discussed and commented on the manuscript.

Conflicts of interest

There are no conflicts to declare.

Acknowledgements

This work was supported by the National Natural Science Foundation of China (42107085), the College Outstanding Young Scientific and Technological Innovation Team of Hubei Province (T201922), and the State Key Laboratory for Modification of Chemical Fibers and Polymer Materials (KF2317).

Notes and references

1 T. Tao and K. A. Xin, *Nature*, 2014, **511**, 527.
2 M. C. Cameron and C. W. Suzanne, *Frontiers in water*, 2022, **4**, 1.
3 C. Kannan, K. Muthuraja and M. R. Devi, *J. Hazard. Mater.*, 2013, **244**, 10.
4 W. Lei, D. Portehault, D. Liu, S. Qin and Y. Chen, *Nat. Commun.*, 2013, **4**, 1777.
5 C. L. Zou, W. Jiang, J. Y. Liang, X. H. Sun and Y. Y. Guan, *Environ. Sci. Pollut. Res.*, 2019, **26**, 1315.
6 R. Das, C. D. Vecitis, A. Schulze, B. Cao, A. Ismail, X. Lu, J. Chene and S. Ramakrishna, *Chem. Soc. Rev.*, 2017, **46**, 6946.
7 A. Mazaher, A. Samira, M. Mohsen and A. H. S. Hesam, *Anal. Bioanal. Chem. Res.*, 2023, **10**, 1.
8 S. J. Tesh and T. B. Scott, *Adv. Mater.*, 2014, **26**, 6056.
9 G. A. Tofik, B. Dejene, E. Million and K. Goshu, *Int. J. Anal. Chem.*, 2022, **1**, 1.
10 J. Zhang, L. Xia, R. Han and W. Wei, *Nat., Environ. Pollut. Technol.*, 2022, **21**, 1.
11 E. Asuquo, A. Martin, P. Nzerem, F. Siperstein and X. L. Fan, *J. Environ. Chem. Eng.*, 2017, **5**, 679.
12 J. C. Xie, X. H. Wang and Q. C. Xu, *Mater. Technol.*, 2012, **27**, 337.
13 E. Qada, N. A. Emad and J. W. Stephen, *Chem. Eng. J.*, 2008, **135**, 74.
14 S. J. Yu, X. X. Wang, H. W. Pang, R. Zhang, W. C. Song, D. Fu, T. Hayat and X. K. Wang, *Chem. Eng. J.*, 2018, **333**, 343.
15 Q. Q. Song, Y. Fang, Z. Y. Liu, L. L. Li, Y. R. Wang, J. L. Liang, Y. Huang, J. Lin, L. Hu, J. Zhang and C. Tang, *Chem. Eng. J.*, 2017, **325**, 71.
16 J. Li, M. T. Xia, L. Zhang, J. H. Tao, C. H. Wang and T. Wu, *Funct. Mater. Lett.*, 2022, **15**, 2251099.
17 Y. Zhang, R. Guo, D. Wang, X. Sun and Z. Xu, *Colloids Surf., B*, 2019, **176**, 300.

18 C. Zhou, C. Lai, C. Zhang, G. Zeng, D. Huang, M. Cheng, L. Hu, W. Xiong, M. Chen, J. Wang, Y. Yang and L. Jiang, *Appl. Catal., B*, 2018, **238**, 6.
19 Q. Weng, X. Wang, X. Wang, Y. Bandoa and D. Golberg, *Chem. Soc. Rev.*, 2016, **45**, 3989.
20 X. Q. Chen, S. J. Fan, C. Han, T. Wu, L. J. Wang, W. Jiang, W. Dai and J. P. Yang, *Rare Met.*, 2021, **40**, 2017.
21 J. Li, Y. Huang, Z. Liu, J. Zhang, X. Liu, H. Luo, Y. Ma, X. Xu, Y. Lu, J. Lin, J. Zuo and C. Tang, *J. Mater. Chem. A*, 2015, **3**, 8185.
22 Q. Zhang, Z. Li, X. Li, L. Yu, Z. Zhang and Z. Wu, *Chem. Eng. J.*, 2019, **356**, 680.
23 W. J. Wang, J. Lin, C. F. Xing, R. Chai, S. Abbas, T. Song, C. Tang and Y. Huang, *Ceram. Int.*, 2017, **43**, 6371.
24 C. T. Yavuz, J. T. Mayo, W. W. Yu, A. Prakash, J. C. Falkner, S. Yean, L. L. Cong, H. J. Shipley, A. Kan, M. Tomson, D. Natelson and V. L. Colvin, *Science*, 2006, **314**, 964–967.
25 R. T. Paine and C. K. Narula, *Chem. Rev.*, 1990, **90**, 73.
26 Q. Weng, X. Wang, C. Zhi, Y. Bando and D. Golberg, *ACS Nano*, 2013, **7**, 1558.
27 X. Zhang, Y. Huang, X. He, J. Lin, X. Yang, D. Li, M. Yu, C. Yu and C. Tang, *Colloids Surf., A*, 2020, **589**, 1.
28 C. Tang, Y. Bando, Y. Huang, C. Zhi and D. Golberg, *Adv. Funct. Mater.*, 2008, **18**, 3653.
29 C. Zhi, Y. Bando, C. Tang, D. Golberg, R. Xie and T. Sekigushi, *Appl. Phys. Lett.*, 2005, **86**, 213110.
30 J. Li, S. He, W. Dai, T. Wu, R. Li, H. Qi, J. Tao, L. Zhang, Y. Zhang, Q. Huang and Y. Tian, *Mater. Technol.*, 2021, **36**, 731.
31 X. Fu, Y. Hu, Y. Yang, W. Liu and S. Chen, *J. Hazard. Mater.*, 2013, **244–245**, 102.
32 X. Fu, Y. Hu, T. Zhang and S. Chen, *Appl. Surf. Sci.*, 2013, **280**, 828.
33 K. S. W. Sing, *Pure Appl. Chem.*, 1985, **57**, 603.
34 S. Brunauer, P. H. Emmett and E. Teller, *J. Am. Chem. Soc.*, 1938, **60**, 309.
35 R. Evans and P. Tarazona, *Phys. Rev. Lett.*, 1984, **52**, 557.
36 J. Li, S. He, R. Li, W. Dai, J. Tao, C. Wang, J. Liu, T. Wu and C. Tang, *RSC Adv.*, 2018, **8**, 32886.
37 Y. Huang, J. Lin, Y. Bando, C. Tang, C. Zhi, Y. Shi, E. T. Muromachi and D. Golberg, *J. Mater. Chem.*, 2010, **20**, 1007.
38 P. Singla, N. Goel, V. kumar and S. Singhal, *Ceram. Int.*, 2015, **41**, 10565.
39 J. Li, P. Lin, W. Dai, C. H. Wang, R. Li, T. Wu and C. Tang, *Mater. Chem. Phys.*, 2017, **196**, 186.
40 J. Lin, L. Xu, Y. Huang, J. Li, W. Wang, C. Feng, Z. Liu, X. Xu, J. Zou and C. Tang, *RSC Adv.*, 2016, **6**, 1253.
41 M. Maleki, A. Beitollahi, J. Javadpour and N. Yahya, *Ceram. Int.*, 2015, **41**, 3806.